

In-plane negative magnetoresistance and quantum oscillations in van der Waals antiferromagnet $DyTe_3$

Qi Qi(齐琦), Senhao Lv(吕森浩), Ke Zhu(祝轲), Yaofeng Xie(谢耀锋), Guojing Hu(胡国静), Zhen Zhao(赵振), Guoyu Xian(冼国裕), Yechao Han(韩烨超), Yang Yang(杨洋), Lihong Bao(鲍丽宏), Xiao Lin(林晓), Hui Guo(郭辉), Haitao Yang(杨海涛), and Hong-Jun Gao(高鸿钧)

Citation: Chin. Phys. B, 2025, 34 (**7**): 077305. DOI: 10.1088/1674-1056/adcc87
http://cpb.iphy.ac.cn; http://iopscience.iop.org/cpb

What follows is a list of articles you may be interested in

Scanning tunneling microscopy study on symmetry breaking of charge density wave in FeGe

Jiakang Zhang(张嘉康), Ziyuan Chen(陈子元), Xueliang Wu(吴学良), Mingzhe Li(李明哲), Yuanji Li(李元骥), Ruotong Yin(尹若彤), Jiashuo Gong(巩佳硕), Shiyuan Wang(王适源), Aifeng Wang(王爱峰), Dong-Lai Feng(封东来), and Ya-Jun Yan(闫亚军)

Chin. Phys. B, 2025, 34 (**4**): 047303. DOI: 10.1088/1674-1056/adb389

Magnetic and electrical transport properties in GdAlSi and SmAlGe

Jing Gong(巩静), Huan Wang(王欢), Xiao-Ping Ma(马小平), Xiang-Yu Zeng(曾祥雨), Jun-Fa Lin(林浚发), Kun Han(韩坤), Yi-Ting Wang(王乙婷), and Tian-Long Xia(夏天龙)

Chin. Phys. B, 2024, 33 (**7**): 077302. DOI: 10.1088/1674-1056/ad41ba

Symmetry transformation of nonlinear optical current of tilted Weyl nodes and application to ferromagnetic $MnBi_2Te_4$

Zhuo-Cheng Lu(卢倬成) and Ji Feng(冯济)

Chin. Phys. B, 2024, 33 (**4**): 047303. DOI: 10.1088/1674-1056/ad2bfb

Quantization of the band at the surface of charge density wave material 2H-$TaSe_2$

Man Li(李满), Nan Xu(徐楠), Jianfeng Zhang(张建丰), Rui Lou(娄睿), Ming Shi(史明), Lijun Li(黎丽君), Hechang Lei(雷和畅), Cedomir Petrovic, Zhonghao Liu(刘中灏), Kai Liu(刘凯), Yaobo Huang(黄耀波), and Shancai Wang(王善才)

Chin. Phys. B, 2021, 30 (**4**): 047305. DOI: 10.1088/1674-1056/abe9a8

Tunable charge density wave in TiS_3 nanoribbons

Ce Huang(黄策), Enze Zhang(张恩泽), Xiang Yuan(袁翔), Weiyi Wang(王伟懿), Yanwen Liu(刘彦闻), Cheng Zhang(张成), Jiwei Ling(凌霁玮), Shanshan Liu(刘姗姗), Faxian Xiu(修发贤)

Chin. Phys. B, 2017, 26 (**6**): 067302. DOI: 10.1088/1674-1056/26/6/067302

RAPID COMMUNICATION

In-plane negative magnetoresistance and quantum oscillations in van der Waals antiferromagnet $DyTe_3$

Qi Qi(齐琦)[1,2,†], Senhao Lv(吕森浩)[1,†], Ke Zhu(祝轲)[1,2], Yaofeng Xie(谢耀锋)[1,2], Guojing Hu(胡国静)[1], Zhen Zhao(赵振)[1], Guoyu Xian(冼国裕)[3], Yechao Han(韩烨超)[2], Yang Yang(杨洋)[1,2], Lihong Bao(鲍丽宏)[1,2], Xiao Lin(林晓)[2], Hui Guo(郭辉)[1,2,‡], Haitao Yang(杨海涛)[1,2,§], and Hong-Jun Gao(高鸿钧)[1,2]

[1] *Beijing National Center for Condensed Matter Physics and Institute of Physics, Chinese Academy of Sciences, Beijing* 100190, *China*
[2] *School of Physical Sciences, University of Chinese Academy of Sciences, Beijing* 100049, *China*
[3] *Songshan Lake Materials Laboratory, Dongguan* 523808, *China*

(Received 8 February 2025; revised manuscript received 6 March 2025; accepted manuscript online 15 April 2025)

Two-dimensional van der Waals (vdW) magnetic materials, characterized by their tunable magnetism, spin transport properties, and remarkable quantum effects, provide significant promise for the development of efficient, low-power spintronic devices. Intriguingly, the rare earth tritelluride (RTe$_3$) materials have attracted great attention due to their unique magnetic structure, exotic electronic properties, multiple charge density wave (CDW), and superconductivity under pressure. Here, we report the successful synthesis of high-quality $DyTe_3$ single crystals using a self-flux method. $DyTe_3$ shows an antiferromagnetic transition at 4.5 K and demonstrates the magnetic field-induced ferromagnetism. The high-quality $DyTe_3$ single crystal demonstrates outstanding transport properties, featuring a high carrier mobility of approximately 1.4×10^4 cm$^2\cdot$V$^{-1}\cdot$s^{-1} and large linear magnetoresistance of 1300%. Furthermore, distinct Shubnikov–de Haas (SdH) oscillations are observed in $DyTe_3$, revealing a small Fermi pocket and an effective mass of 0.24 m_e. Remarkably, the unconventional in-plane negative magnetoresistances appear along the a-axis below 2 T and c-axis until 9 T from 2 K to 17 K, which are attributed to the complex helimagnetic structures caused by CDW coupling and weak single-ion anisotropy. Our findings offer a significant platform for understanding the complex magnetoresistance behavior and quantum transport effects in RTe$_3$-type materials, holding great promise for advancing applications in electronic and spintronic devices.

Keywords: in-plane negative magnetoresistance, SdH oscillations, helimagnetic, charge density wave (CDW)

PACS: 73.43.Qt

DOI: 10.1088/1674-1056/adcc87 **CSTR:** 32038.14.CPB.adcc87

1. Introduction

Two-dimensional (2D) van der Waals (vdW) materials[1–3] encompass diverse electrical properties, including metallic,[4] semi-metallic,[5] semiconductive,[6,7] insulating,[8] and superconductive.[9] Their unique properties pave the way for overcoming the limitations of Moore's law, facilitating the development of advanced low-dimensional electronic devices. The emergence of vdW magnetic materials provides an unprecedented platform for exploring the fundamental 2D magnetism and modulating spin-related effect, paving the way for promising applications in low-power 2D spintronics.[10] Unlike conventional bulk magnets, these materials such as CrX_3 (X = Cl, Br, I),[11–13] $Cr_2Ge_2Te_6$,[14] Fe_3GeTe_2,[2] Fe_3GaTe_2,[15] $FePS_3$,[16] $CrPS_4$,[17] $RuCl_3$,[18] retain intrinsic long-range magnetic order down to the atomic-level thickness. Moreover, 2D vdW magnetic materials can overcome lattice matching limitations through vdW interactions to enable the construction of various heterostructures, providing new prospects for high-performance magnetic sensors and non-volatile memory devices. Thus, the exploration of new 2D vdW magnetic materials with special magnetic properties and their underlying physical mechanisms plays a crucial role to accomplish the construction of 2D spintronic devices.

Of particular interest, the RTe$_3$ family (R = Y, La, Ce, Pr, Nd, Sm, Gd, Tb, Dy, Ho, Er, and Tm) combines the 4f electrons of rare-earth atoms with strong spin–orbital coupling of Te, exhibiting high carrier density, excellent mobility,[19] and intrinsic magnetism,[20,21] making them promising candidates for electronic, spintronic, and novel magnetic device applications. Furthermore, as an important characteristic of the RTe$_3$ family materials, charge density wave (CDW) can be modulated by changes in rare-earth atoms[22] and external stress,[23] providing an ideal platform for studying electron correlated states and phase transitions. Notably, superconductivity emerges with the suppression of CDW by the pressure (in $GdTe_3$, $TbTe_3$, and $DyTe_3$)[24] or Pd intercalation (in $ErTe_3$),[25] highlighting the competition between CDW and superconductivity. Among the RTe$_3$-type

†These authors contributed equally to this work.
‡Corresponding author. E-mail: guohui@iphy.ac.cn
§Corresponding author. E-mail: htyang@iphy.ac.cn

© 2025 Chinese Physical Society and IOP Publishing Ltd. All rights, including for text and data mining, AI training, and similar technologies, are reserved.

materials, $DyTe_3$ stands out due to its unique helimagnetic structure,[20] the largest magnetic moment among lanthanide rare-earth ions,[20] and its exotic electronic structures including the Brillouin zone folding and the gapping of the Fermi surface induced by the double CDW.[26] Recently, it has been found that $DyTe_3$ exhibits multiple CDW,[22] superconductivity under pressure,[24] non-coplanar helimagnetism and competing interactions between the CDW-driven term in the one-dimensional spin model and antiferromagnetism.[20] However, its in-plane magnetoresistances and quantum effects such as Shubnikov–de Haas (SdH) oscillations are still rarely studied.

In this article, we report the synthesis of high-quality $DyTe_3$ single crystal by using a self-flux method. The magnetic measurements demonstrate that $DyTe_3$ undergoes an antiferromagnetic transition at 4.5 K and exhibits field-induced ferromagnetic order. Low-temperature magneto-transport measurements reveal that the high-quality $DyTe_3$ exhibits a large linear magnetoresistance of 1300% under 15 T and an ultrahigh carrier mobility of 14059 $cm^2 \cdot V^{-1} \cdot s^{-1}$ at 2 K. Furthermore, clear SdH oscillations have been detected with a low onset magnetic field of 6 T. Remarkably, the in-plane negative magnetoresistance (MR) is induced by complex helimagnetic structures caused by CDW coupling and weak single-ion anisotropy. Our work provides a valuable platform for exploring their rich magnetoresistance behavior and understanding quantum transport effects in RTe_3-type materials, with the promise of facilitating the development of spintronic devices in future technologies.

2. Experimental method

2.1. Synthesis method

The $DyTe_3$ single crystal was synthesized by a self-flux method.[23,24,27] Dy and Te elements with a ratio of 1:30 were placed in an Al_2O_3 crucible, and then sealed in a quartz tube. The quartz tube was heated to 900 °C and kept for 48 h and then cooled down slowly to 550 °C over 175 h, followed by a separation process of single crystals and flux via a centrifugation treatment.

2.2. Sample characterizations

XRD patterns were collected by a Rigaku SmartLab SE x-ray diffractometer with Cu $K\alpha$ radiation ($\lambda = 0.15418$ nm) at room temperature. A Bruker D8 VentureSingle was employed to obtain crystal diffraction patterns. Scanning electron microscopy (SEM) and x-ray energy-dispersive spectroscopy (EDS) were taken by a HITACHI S5000 with an energy dispersive analysis system Bruker XFlash 6|60. Magnetization measurements were carried out on single crystals by a vibrating sample magnetometer (MPMS 3, Quantum Design). Electrical transport measurements were conducted using a Quantum Design physical properties measurement system (PPMS).

3. Structure characterizations of $DyTe_3$ single crystals

$DyTe_3$, as a member of the RTe_3 family (R = Y, La, Ce, Pr, Nd, Sm, Gd, Tb, Dy, Ho, Er, and Tm), shares similar

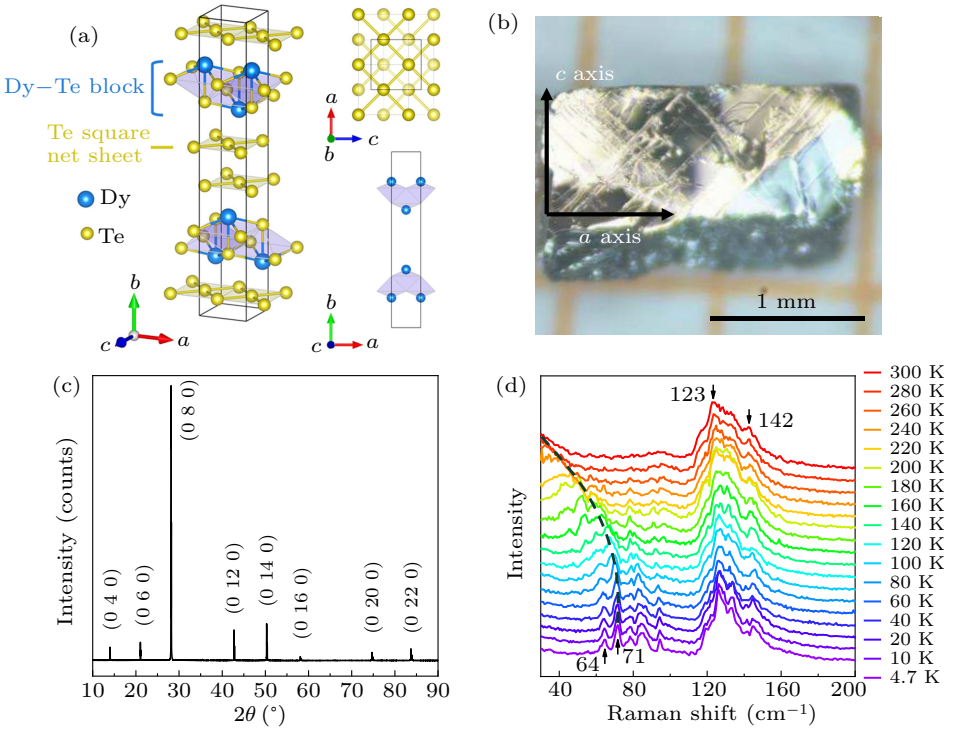


Fig. 1. Structure characterizations of $DyTe_3$ single crystals. (a) Crystal structure of $DyTe_3$, where Dy–Te block layers are sandwiched between the square-net sheets formed by Te atoms. (b) A typical photography of $DyTe_3$ single crystal with a metallic luster, showing a regular rectangle with a long side along a-axis and a short side along c-axis. (c) The XRD pattern of the $DyTe_3$ single crystal exhibits diffraction peaks corresponding to the [0/0] crystal planes, indicating a high crystalline quality. (d) A typical temperature-dependent Raman spectra of $DyTe_3$ single crystal from 300 K to 4.7 K, showing an obvious evolution of the peak corresponding to CDW.

orthorhombic crystal structures with *cmcm* space group symmetry,[27] as shown in Fig. 1(a). The lattice constants of $DyTe_3$ are $a = 4.302$ Å, $b = 25.45$ Å, and $c = 4.304$ Å.[4] In the unit cell, an insulating Dy–Te block layer is sandwiched between two metallic Te square net sheets,[4,20] which are held together by vdW forces.[27] Figure 1(b) shows an optical photograph of a typical $DyTe_3$ single crystal, with dimensions of 2 mm×1 mm×0.2 mm, clearly showcasing a rectangular shape. The crystal orientation was determined by the single-crystal diffraction, as marked in Fig. 1(b), and the freshly cleaved surface exhibits a golden color with a metallic luster. The x-ray energy dispersive spectroscopy reveals a uniform distribution of Dy and Te elements, with a stoichiometric ratio of Dy:Te of approximately 1:3, as shown in Fig. S1. The x-ray diffraction (XRD) pattern in Fig. 1(c) shows only the (0*l*0) diffraction peaks,[26,28] confirming the pure phase and excellent crystalline quality of the as-grown $DyTe_3$ single crystals with a preferred [0*l*0] orientation. The rocking curve from the (080) reflection (Fig. S2(a)) shows a small full-width at half-maximum (FWHM) of $\sim 0.196°$, indicating the high crystalline quality of the as-grown $DyTe_3$ crystals.

A typical temperature-dependent Raman spectrum of the $DyTe_3$ single crystal is shown in Fig. 1(d). In the low-temperature (4.7 K) Raman spectrum fitted with a Lorentzian model (Fig. S2(b)), a transition corresponding to the high-temperature CDW ($T_{CDW} = 307$ K) is observed at low wavenumbers (around 60 cm^{-1} and 70 cm^{-1}).[29,30] From 4.7 K to 300 K, the CDW-related peaks have a large shift of about 40 cm^{-1}, while the peaks at higher wavenumbers corresponding to the lattice vibration have a slight shift of about 2 cm^{-1}. This reveals that the CDW is caused by the nesting of Fermi surface rather than lattice vibration.[22]

4. Magnetic properties of $DyTe_3$ single crystals

The magnetic ground state of $DyTe_3$ is helimagnetic with cone-type orders caused by CDW coupling and weak single-ion anisotropy, as confirmed by polarized elastic neutron scattering.[20] The temperature-dependent magnetization was measured with various fields (B) applied parallel to the b-axis, as shown in Figs. 2(a) and S3(a), revealing an antiferromagnetic transition at 4.5 K ($T_N = 4.5$ K). Interestingly, as the applied magnetic field increases to 0.8 T, the antiferromagnetic transition temperature shifts to lower temperatures, and a noticeable bifurcation between the ZFC and FC curves emerges at low temperatures (as indicated by the dashed circle in the inset of Fig. 2(a)), suggesting the presence of field-induced weak ferromagnetic order. With the further increase of the applied magnetic field, the antiferromagnetic order is suppressed, giving rise to the field-induced ferromagnetism. The temperature-dependent magnetic susceptibility (χ) was measured at 0.01 T with the field applied along the a, b, and c axis, showing an anisotropic magnetic behavior (Fig. 2(b)). And the $1/\chi$ versus T (temperature) curve, fitted by the Curie–Weiss law at $B = 0.01$ T along the b-axis (Fig. S3(b)), reveals an effective magnetic moment of 10.97 μ_B per Dy, closely matching the theoretical value of 10.63 μ_B.[21] The $1/\chi$ vs.

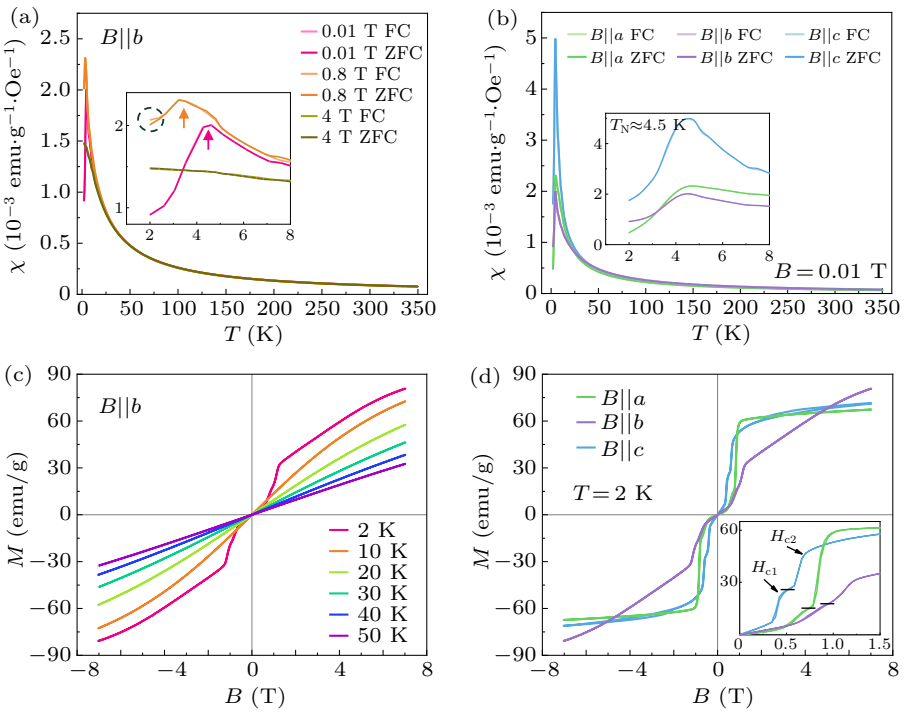


Fig. 2. Magnetic properties of $DyTe_3$ single crystals. (a) Temperature dependence of susceptibility under the applied magnetic field along the b-axis. The inset displays an enlarged part from 2 K to 8 K, revealing an antiferromagnetic transition at 4.5 K. (b) Temperature dependence of susceptibility measured under a field of $B = 0.01$ T along the a-, b-, and c-axis respectively. The inset shows an enlarged region from 2 K to 8 K, highlighting an antiferromagnetic transition at 4.5 K along the different axes. (c) Magnetic field dependence of the magnetization along the b-axis, showing two transitions with critical fields of 0.8 T and 1.1 T. (d) The magnetization at 2 K under an applied field along a-, b, and c-axis, showing two critical fields in all three directions.

temperature curve and the corresponding Curie–Weiss fitting curve at $B = 6$ T along the b-axis, as shown in Fig. S3(c), reveal a deviation from the fitting around 150 K upon cooling, which indicates the persistence of the ferromagnetic order in a broad temperature range above T_N under high fields.

The field-dependent magnetization (M–H) with the field along the b-axis at temperatures from 2 K to 50 K reveals two transitions at the critical fields of 0.8 T and 1.1 T at 2 K, with a distinct paramagnetic behavior observed as the temperature increases (Fig. 2(c)). The field dependence of magnetization with the field along the a, b, and c axis displays a strong anisotropic magnetic behavior (Figs. 2(c) and S4), with the easy magnetization axis along the c-axis. The effective magnetic moments fitted by the Curie–Weiss law along the c and a-axes are $m(c) = 10.51$ μ_B/Dy and $m(a) = 10.10$ μ_B/Dy, respectively. And under 7 T, the magnetic moment reaches 7.28 μ_B/Dy (69% of the saturation magnetization M_s) when $B \parallel c$, while it reaches 6.86 μ_B/Dy (68% of M_s) when $B \parallel a$. Notably, the magnetization along the b-axis does not saturate due to the hard magnetization axis until 7 T, while the magnetization along the a- and c-axis exhibits a small plateau at $\sim 1/4M_s$, which may result from a complex multi-phase magnetic structure related to the helimagnetic ground state.

5. High mobility and SdH oscillations of $DyTe_3$ single crystals

Then we further study the electrical transport properties of $DyTe_3$ single crystals. The temperature-dependent resistivity under various fields (Fig. 3(a)) exhibits the metallic behavior across the entire temperature range from 1.9 K to 350 K,[21,24] with a residual resistivity ratio (RRR) of ~ 77, indicating a relatively high quality of $DyTe_3$ crystals. A hump-like transition at 307 K, corresponding to the CDW transition of $DyTe_3$, is observed and remains robust under the applied field along the b-axis. While another hump-like transition around 50 K is also observed (Fig. S5), which is possibly due to a second CDW transition at low temperatures, similar to the previous results.[22] Figure 3(b) shows the field-dependent ρ_{yx} at temperatures from 1.9 K to 100 K in an out-of-plane configuration with $B \parallel b$, exhibiting the nonlinear behavior up to 50 K, indicating the typical characteristic of multi-type carriers. Therefore, we apply the following two-band model[19,31] to extract the carrier concentration and mobility:

$$\sigma_{xx} = en_h n_h \frac{1}{1+(\mu_h B)^2} + en_e n_e \frac{1}{1+(\mu_e B)^2},$$

$$\sigma_{xy} = \left[n_h \mu_h^2 \frac{1}{1+(\mu_h B)^2} - n_e \mu_e^2 \frac{1}{1+(\mu_e B)^2} \right] eB,$$

where σ_{xx} and σ_{xy} represent the longitudinal conductivity and Hall conductivity, n_h and n_e denote the carrier density of hole and electron, μ_h and μ_e correspond to the carrier mobility of hole and electron, B refers to the applied magnetic field. According to the fitting results with the two-band model (Fig. S6(a)), the carrier mobilities of electrons and holes are approximately 14059 $cm^2 \cdot V^{-1} \cdot s^{-1}$ and 2878 $cm^2 \cdot V^{-1} \cdot s^{-1}$ at 2 K, respectively, and decrease with increasing temperature, as shown in Fig. 3(c), while the corresponding carrier densities are $n_h = 1.3 \times 10^{21}$ cm^{-3} and $n_e = 5.3 \times 10^{20}$ cm^{-3}. The carrier mobility in our $DyTe_3$ crystals shows a large value, comparable to 15000 $cm^2 \cdot V^{-1} \cdot s^{-1}$ for graphene on a SiO_2 substrate[32] and $\sim 10^4$ $cm^2 \cdot V^{-1} \cdot s^{-1}$ for black phosphorus.[33]

Figure 3(d) shows the magnetic-field dependent magnetoresistance for the $DyTe_3$ under the out-of-plane fields at different temperatures from 1.9 K to 50 K. Above 20 K, the magnetoresistance transitions to a conventional dependence approximately proportional to B^2 (Fig. S6(b)). At low temperatures (≤ 10 K), a pronounced linear behavior can be observed with a maximum magnetoresistance of 1300% under 15 T at 2 K. Several mechanisms have been proposed to explain linear magnetoresistance, including Abrikosov's quantum model,[34,35] the Parish–Littlewood (PL) model,[36] the interplay between the momentum-space Berry curvature and real-space magnetic field, which causes carriers to slow down linearly,[37] and the presence of specific hot spots near the Fermi surface.[38] The measured carrier density of $DyTe_3$ at 1.9 K is $\sim 10^{21}$ cm^{-3}, exceeding the range of applicability for Abrikosov theory.[31] Since the PL model describes inhomogeneous systems, it is not suitable for the explanation of the linear MR in $DyTe_3$, which is a homogeneous system conformed by the sharp XRD peaks and high RRR of ~ 77. A more plausible origin of the linear positive magnetoresistance is the potential presence of Weyl points in the field-induced ferromagnetic state (> 1 T),[39] where the Berry curvature and the magnetic field interact. In addition, the theoretical calculation speculates that the origin of linear MR comes from the scattering induced by specific hot spots.

Interestingly, multiple plateaus are observed in the high-field region (above ~ 6 T) of the magnetoresistance curves, indicating the presence of SdH oscillations in the high-mobility $DyTe_3$ single crystal.[19,40] And the SdH oscillations become clearly visible by subtracting a polynomial background from the data as shown in Fig. 3(e). Generally, the SdH oscillation can be described by the Lifshitz–Kosevich (LK) formula[41–43]

$$\Delta R \propto \frac{\lambda T}{\sinh(\lambda T)} e^{-\lambda T_D} \cos\left[2\pi\left(\frac{F}{B} - \frac{1}{2} + \beta + \delta\right)\right],$$

where $\lambda = 2\pi^2 k_B m^*/(\hbar e B)$, k_B denotes the Boltzmann constant, $\hbar$ represents the reduced Planck constant, T is the temperature, T_D is the Dingle temperature, F corresponds to the oscillation frequency, and m^* is the effective mass, $2\pi\beta$ represents the Berry phase and δ is a phase shift, equal to 0 for 2D systems or $\pm 1/8$ for 3D systems.

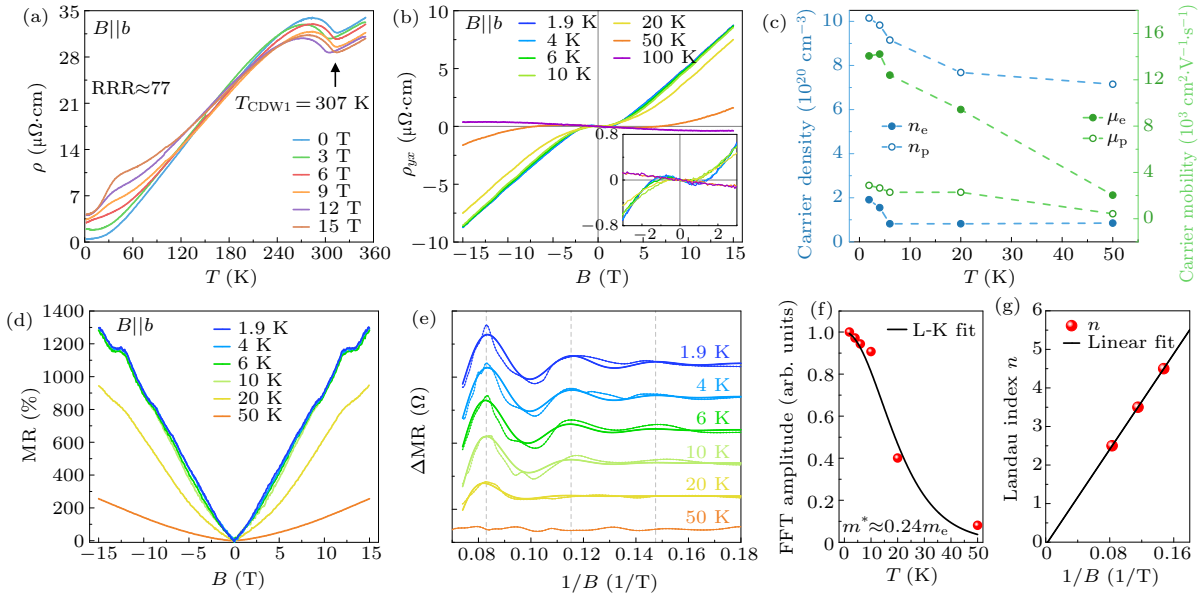


Fig. 3. Quantum oscillations of $DyTe_3$ single crystals. (a) Temperature dependence of resistivity under the various applied magnetic fields along *b*-axis. (b) Magnetic field dependence of Hall resistivity at various temperatures from 1.9 K to 100 K. (c) Temperature dependence of the carrier density (n) and mobility (μ) extracted using the two-band model. (d) Magnetic field dependence of MR at various temperatures from 1.9 K to 50 K, showing the linear MR and SdH oscillations. (e) SdH oscillations after a smooth subtraction of background at various temperatures, with solid lines representing fitting curves based on the L-K formula. (f) Temperature dependence of the normalized FFT amplitude, with the frequency of 31 T. The extracted effective mass is 0.24 m_e. (g) Landau fan diagram with the linear fitting, showing an intercept near 0.

The oscillation frequency F is determined through fast Fourier transformation (FFT) analysis of the oscillations at various temperatures, yielding an F value of 31 T in $DyTe_3$ (Fig. S7). And the effective mass m^* is extracted by fitting the temperature-dependent oscillation amplitude at a fixed field using the L-K temperature reduction factor (Fig. 3(f))

$$R_T = \frac{\lambda T}{\sinh(\lambda T)}.$$

Here, the amplitude of FFT at 31 T is chosen to be normalized and fitted, getting an effective mass m^* of 0.24 m_e (m_e is the mass of an electron). A Dingle temperature T_D of 10.93 K is obtained by the slope of linear fitting of $\ln(\Delta R \cdot B \cdot \sinh(\lambda T))$ vs. $1/B$. The oscillations at various temperatures are fitted using the L-K formula, showing a good consistency with the experimental data, as shown in Fig. 3(e). The following parameters can also be derived. The cross-sectional area of the Fermi pocket normal to the field is $A_F = \frac{2\pi e}{\hbar} \cdot F = 0.003$ Å^{-2}, a relatively small value, which is attributed to the folding of the Brillouin zone and the gapping of the Fermi surface by the double CDW.[40] The other parameters are also obtained: Fermi wave vector $k_F = 0.031$ Å^{-1}; Fermi velocity $v_F = \hbar k_F/m^* = 1.50 \times 10^5$ m/s; Fermi energy $E_F = (\hbar k_F)^2/m^* = 48.9$ meV; quantum scattering time $\tau = \hbar/(2\pi k_B T_D) = 1.11 \times 10^{-13}$ s; quantum mobility $\mu_q = e \cdot \tau/m^* = 813$ cm^2·V^{-1}·s^{-1}; and mean free path $l_q = v_F \cdot \tau = 16.7$ nm. And we note a discrepancy between the transport and quantum mobilities, which can be attributed to the distinct scattering mechanisms underlying each type of mobility. Transport mobility is mainly influenced by large-angle scattering, whereas quantum mobility reflects all scattering events that contribute to Landau level broadening, including small-angle scattering.[44,45] As a result, the mean free path associated with momentum relaxation is typically longer than that related to Landau level broadening, thereby resulting in quantum mobility being intrinsically lower than transport mobility.

In addition, a Landau fan diagram is constructed in Fig. 3(f), with the intercept of the Landau index (n) axis near zero, indicating a trivial energy band. The Landau index is determined after the determining frequency F by FFT of the oscillations, for $\beta = 0$, valleys appear at $B = F$, 1/2 F, 1/3 F, ..., corresponding to Landau level indices $n = 1, 2, 3, \ldots$.

6. In-plane negative magnetoresistance

Next, the direction of the applied magnetic field was then altered to be parallel to the a-axis ($B \parallel I$) or the c-axis ($B \perp I$), while the current direction was kept constant, and the field-dependent MR was measured at various temperatures. The magnetic-field dependence of magnetoresistance with $B \parallel I$ ($B \parallel a$) in the low temperature ranging from 2 K to 4 K (below T_N) exhibits a negative magnetoresistance below 2 T and a linear unsaturated positive magnetoresistance at higher fields above 2 T (Fig. 4(a)). A sharp transition is observed around 2 T, mainly due to the changes in the electron scattering rate induced by a ferromagnetic transition. As the temperature increases from T_N to 17 K, the field-dependent magnetoresistance curve exhibits the complex negative magnetoresistance behavior with a transition from the negative to positive slope, where the corresponding magnetic fields shift to higher values

(Fig. 4(b)). While above 20 K, it shows an unsaturated positive magnetoresistance effect (Fig. 4(c)). Figure 4(d) shows the magnetic-field dependence of magnetoresistance with $B \perp I$ ($B \parallel c$) at different temperatures from 2 K to 4 K, with a distinct kink around 2 T. As the temperature increases, the negative magnetoresistance effect initially grows and then diminishes, reaching a maximum of 25% under 9 T at 6 K (Figs. 4(e) and 4(f)).

Several common origins of negative magnetoresistance (MR) have been proposed, including the Kondo effect, weak localization,[46] chiral anomaly,[47] and magnetic scattering.[48] The negative MR induced by the Kondo effect typically follows a behavior of MR $\propto B^2$, which is not observed in this sample, thus ruling out the Kondo effect as the origin. In the case of the weak localization (WL) in 2D system, the resistivity should exhibit a logarithmic temperature dependence, $\sigma \propto \ln(T)$. However, in our results, the resistivity follows $\rho \propto T^2$ below 20 K, indicating the presence of electron-electron interactions, as shown in Fig. S5. This observation excludes WL as a contributing factor. Negative MR attributed to chiral anomaly is particularly sensitive to the angle between the applied magnetic field and the current direction, typically manifesting when $B \parallel I$ and disappearing when $B \perp I$. However, in our case, this behavior is only observed when the magnetic field is less than 0.5 T and the temperature is below 4 K. Moreover, since the ground state of $DyTe_3$ is metallic rather than a topological semimetal, the chiral anomaly cannot be the origin of the negative MR. After considering the magnetic structure discussed earlier, it is reasonable to conclude that the negative MR in $DyTe_3$ is primarily caused by complex helimagnetic structures induced by CDW coupling and weak single-ion anisotropy.

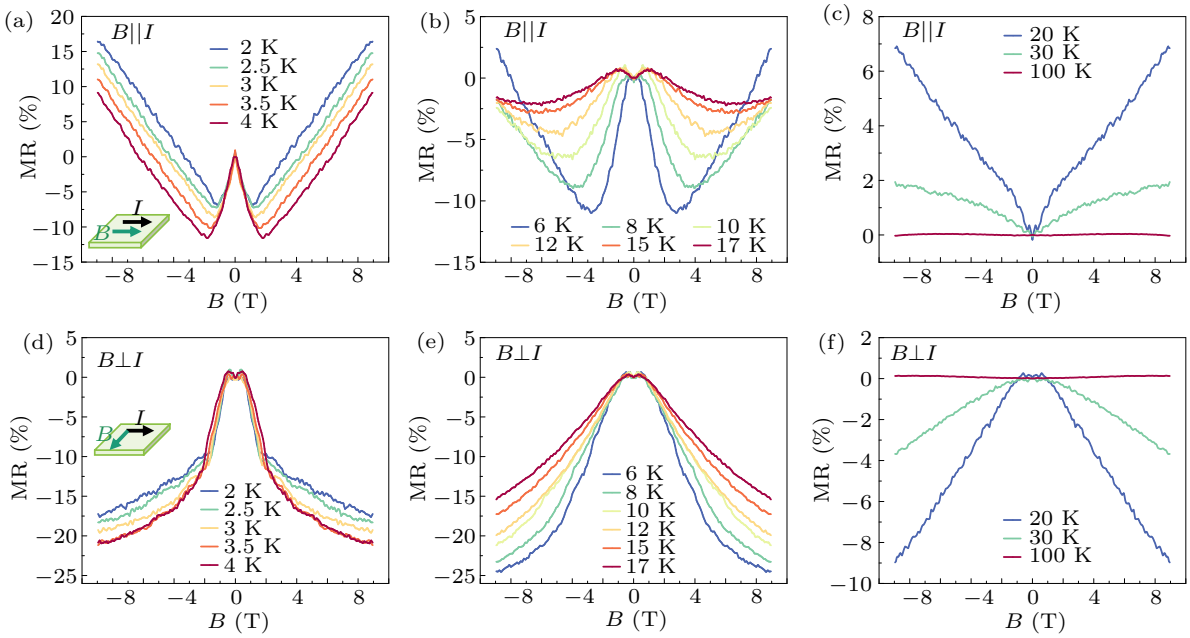


Fig. 4. In-plane negative MR of $DyTe_3$ single crystals. (a)–(c) Field dependence of the in-plane MR under the applied fields up to 9 T at different temperatures from 2 K to 100 K for $B \parallel I$, exhibiting a negative MR below 20 K and non-saturated positive magnetoresistance above 20 K. (d)–(f) Field dependence of the in-plane MR under the applied fields up to 9 T at different temperatures from 2 K to 100 K for $B \perp I$, showing an unsaturated negative MR effect in the temperature range from 2 K to 30 K, with the maximum negative MR reaching 25% at 6 K.

7. Conclusion

In summary, we have successfully synthesized high-quality $DyTe_3$ single crystals with excellent crystallinity using the self-flux method. Magnetic measurements reveal that $DyTe_3$ shows an antiferromagnetic transition at 4.5 K and develops a field-induced ferromagnetic order. And the high-quality $DyTe_3$ single crystal exhibits excellent transport properties, including a high carrier mobility and large linear magnetoresistance of $\sim 1.4 \times 10^4$ $cm^2 \cdot V^{-1} \cdot s^{-1}$, 1300%, respectively. Interestingly, SdH oscillations are observed in $DyTe_3$, with an analysis based on the Lifshitz–Kosevich (L-K) formula revealing a small Fermi pocket ($A_F = 0.003$ Å^{-2}) and an effective mass of 0.24 m_e, while the Landau fan diagram shows an intercept near zero, suggesting a trivial energy band. Remarkably, based on the anisotropic magnetic properties along the three crystal axes, the in-plane magnetoresistances exhibit an unconventional negative magnetoresistance behavior at low temperatures, which is attributed to the complex helimagnetic structures caused by CDW coupling and weak single-ion anisotropy. Our findings provide a key insight into the understanding of intricate magnetoresistance behavior and quantum transport effects in RTe_3-type materials, which is conducive to advancing electronic and spintronic device applications.

Acknowledgements

Project supported by the National Natural Science Foundation of China (Grant Nos. 62488201 and 1240041502), the Ministry of Science and Technology of China (Grant No. 2022YFA1204100), the Chinese Academy of Sciences (Grant No. XDB33030100), and the Innovation Program of Quantum Science and Technology (Grant No. 2021ZD0302700).

References

[1] Ali M N, Xiong J, Flynn S, Tao J, Gibson Q D, Schoop L M, Liang T, Haldolaarachchige N, Hirschberger M, Ong N P and Cava R J 2014 *Nature* **514** 205
[2] Deng Y, Yu Y, Song Y, Zhang J, Wang N Z, Sun Z, Yi Y, Wu Y Z, Wu S, Zhu J, Wang J, Chen X H and Zhang Y 2018 *Nature* **563** 94
[3] Kim K S, Lee D, Chang C S, Seo S, Hu Y, Cha S, Kim H, Shin J, Lee J H, Lee S, Kim J S, Kim K H, Suh J M, Meng Y, Park B I, Lee J H, Park H S, Kum H S, Jo M H, Yeom G Y, Cho K, Park J H, Bae S H and Kim J 2023 *Nature* **614** 88
[4] Brouet V, Yang W L, Zhou X J, Hussain Z, Moore R G, He R, Lu D H, Shen Z X, Laverock J, Dugdale S B, Ru N and Fisher I R 2008 *Phys. Rev. B* **77** 235104
[5] Lee C H, Silva E C, Calderin L, Nguyen M A T, Hollander M J, Bersch B, Mallouk T E and Robinson J A 2015 *Sci. Rep.* **5** 10013
[6] Liu L, Li T, Ma L, Li W, Gao S, Sun W, Dong R, Zou X, Fan D, Shao L, Gu C, Dai N, Yu Z, Chen X, Tu X, Nie Y, Wang P, Wang J, Shi Y and Wang X 2022 *Nature* **605** 69
[7] Li L, Wang Q, Wu F, Xu Q, Tian J, Huang Z, Wang Q, Zhao X, Zhang Q, Fan Q, Li X, Peng Y, Zhang Y, Ji K, Zhi A, Sun H, Zhu M, Zhu J, Lu N, Lu Y, Wang S, Bai X, Xu Y, Yang W, Li N, Shi D, Xian L, Liu K, Du L and Zhang G 2024 *Nat. Commun.* **15** 1825
[8] Wang L, Xu X, Zhang L, Qiao R, Wu M, Wang Z, Zhang S, Liang J, Zhang Z, Zhang Z, Chen W, Xie X, Zong J, Shan Y, Guo Y, Willinger M, Wu H, Li Q, Wang W, Gao P, Wu S, Zhang Y, Jiang Y, Yu D, Wang E, Bai X, Wang Z J, Ding F and Liu K 2019 *Nature* **570** 91
[9] Xi X, Wang Z, Zhao W, Park J H, Law K T, Berger H, Forró L, Shan J and Mak K F 2016 *Nat. Phys.* **12** 139
[10] Li H, Ruan S and Zeng Y 2019 *Adv. Mater.* **31** 1900065
[11] Wang Z, Gibertini M, Dumcenco D, Taniguchi T, Watanabe K, Giannini E and Morpurgo A F 2019 *Nat. Nanotechnol.* **14** 1116
[12] Ghazaryan D, Greenaway M T, Wang Z, Guarochico-Moreira V H, Vera-Marun I J, Yin J, Liao Y, Morozov S V, Kristanovski O, Lichtenstein A I, Katsnelson M I, Withers F, Mishchenko A, Eaves L, Geim A K, Novoselov K S and Misra A 2018 *Nat. Electron.* **1** 344
[13] Huang B, Clark G, Navarro-Moratalla E, Klein D R, Cheng R, Seyler K L, Zhong D, Schmidgall E, McGuire M A, Cobden D H, Yao W, Xiao D, Jarillo-Herrero P and Xu X 2017 *Nature* **546** 270
[14] Gong C, Li L, Li Z, Ji H, Stern A, Xia Y, Cao T, Bao W, Wang C, Wang Y, Qiu Z Q, Cava R J, Louie S G, Xia J and Zhang X 2017 *Nature* **546** 265
[15] Zhang G, Guo F, Wu H, Wen X, Yang L, Jin W, Zhang W and Chang H 2022 *Nat. Commun.* **13** 5067
[16] Lee J U, Lee S, Ryoo J H, Kang S, Kim T Y, Kim P, Park C H, Park J G and Cheong H 2016 *Nano Lett.* **16** 7433
[17] Li Q, Zhen W, Wang N, Shi M, Yu Y, Pan S, Deng L, Cai J, Wang K, Zou L, Zeng Z and Zhang J 2024 *Chin. Phys. Lett.* **41** 107503
[18] Tian Y, Gao W, Henriksen E A, Chelikowsky J R and Yang L 2019 *Nano Lett.* **19** 7673
[19] Lei S, Lin J, Jia Y, Gray M, Topp A, Farahi G, Klemenz S, Gao T, Rodolakis F, McChesney J L, Ast C R, Yazdani A, Burch K S, Wu S, Ong N P and Schoop L M 2020 *Sci. Adv.* **6** eaay6407
[20] Akatsuka S, Esser S, Okumura S, Yambe R, Yamada R, Hirschmann M M, Aji S, White J S, Gao S, Onuki Y, Arima T, Nakajima T and Hirschberger M 2024 *Nat. Commun.* **15** 4291
[21] Iyeiri Y, Okumura T, Michioka C and Suzuki K 2003 *Phys. Rev. B* **67** 144417
[22] Ru N, Condron C L, Margulis G Y, Shin K Y, Laverock J, Dugdale S B, Toney M F and Fisher I R 2008 *Phys. Rev. B* **77** 035114
[23] Straquadine J A W, Ikeda M S and Fisher I R 2022 *Phys. Rev. X* **12** 021046
[24] Zocco D A, Hamlin J J, Grube K, Chu J H, Kuo H H, Fisher I R and Maple M B 2015 *Phys. Rev. B* **91** 205114
[25] Iguchi Y, Straquadine J A, Murthy C, Kivelson S A, Singh A G, Fisher I R and Moler K A 2024 *Phys. Rev. Lett.* **133** 036001
[26] Liu J S, Huan S C, Liu Z H, Liu W L, Liu Z T, Lu X L, Huang Z, Jiang Z C, Wang X, Yu N, Zou Z Q, Guo Y F and Shen D W 2020 *Phys. Rev. Mater.* **4** 114005
[27] Pariari A, Koley S, Roy S, Singha R, Laad M S, Taraphder A and Mandal P 2021 *Phys. Rev. B* **104** 155147
[28] Yumigeta K, Attarde Y, Kopaczek J, Sayyad M Y, Shen Y, Blei M, Rajaei Moosavy S T, Qin Y, Sailus R and Tongay S 2022 *APL Mater.* **10** 111112
[29] Lavagnini M, Eiter H M, Tassini L, Muschler B, Hackl R, Monnier R, Chu J H, Fisher I R and Degiorgi L 2010 *Phys. Rev. B* **81** 081101
[30] Yusupov R V, Mertelj T, Chu J H, Fisher I R and Mihailovic D 2008 *Phys. Rev. Lett.* **101** 246402
[31] Xing Y, Li Y, Yang Z, Wang Z, Yang P, Ge J, Liu Y, Liu Y, Luo T, Tang Y and Wang J 2020 *J. Appl. Phys.* **128** 073901
[32] Ci H, Chen J, Ma H, Sun X, Jiang X, Liu K, Shan J, Lian X, Jiang B, Liu R, Liu B, Yang G, Yin W, Zhao W, Huang L, Gao T, Sun J and Liu Z 2022 *Adv. Mater.* **34** 2206389
[33] He J, He D, Wang Y, Cui Q, Bellus M Z, Chiu H Y and Zhao H 2015 *ACS Nano* **9** 6436
[34] Abrikosov A A 1998 *Phys. Rev. B* **58** 2788
[35] Abrikosov A A 2000 *Europhys. Lett. EPL* **49** 789
[36] Parish M M and Littlewood P B 2003 *Nature* **426** 162
[37] Zhang S, Wang Y, Zeng Q, Shen J, Zheng X, Yang J, Wang Z, Xi C, Wang B, Zhou M, Huang R, Wei H, Yao Y, Wang S, Parkin S S P, Felser C, Liu E and Shen B 2022 *Proc. Natl. Acad. Sci. USA* **119** e2208505119
[38] Sinchenko A A, Grigoriev P D, Lejay P and Monceau P 2017 *Phys. Rev. B* **96** 245129
[39] Wan Y M, Cheng E J, Ma H Y, Yang X F, Hou X F, Chen X J, Zhang X, Xi C Y, Zhong Z C, Liu J P, Guo Y F and Li S Y 2023 *Phys. Rev. B* **108** 205132
[40] Walmsley P, Aeschlimann S, Straquadine J A W, Giraldo-Gallo P, Riggs S C, Chan M K, McDonald R D and Fisher I R 2020 *Phys. Rev. B* **102** 045150
[41] Dalgaard K J, Lei S, Wiedmann S, Bremholm M and Schoop L M 2020 *Phys. Rev. B* **102** 245109
[42] Li L, Ye G J, Tran V, Fei R, Chen G, Wang H, Wang J, Watanabe K, Taniguchi T, Yang L, Chen X H and Zhang Y 2015 *Nat. Nanotechnol.* **10** 608
[43] Zhang L, Pan D, Chen Y, Zhao J and Xu H 2022 *Chin. Phys. B* **31** 098507
[44] Liang T, Gibson Q, Ali M N, Liu M, Cava R J and Ong N P 2015 *Nat. Mater.* **14** 280
[45] Ding L, Koo J, Yi C, Xu L, Zuo H, Yang M, Shi Y, Yan B, Behnia K and Zhu Z 2021 *J. Phys. Appl. Phys.* **54** 454003
[46] Yi Z K, Liu Q, Guang S K, Xu S, Yue X Y, Liang H, Li N, Zhou Y, Wu D D, Sun Y, Li Q J, Cheng P, Xia T L, Sun X F and Wang Y Y 2024 *Chin. Phys. B* **33** 047501
[47] Son D T and Spivak B Z 2013 *Phys. Rev. B* **88** 104412
[48] Karki Chhetri S, Acharya G, Graf D, Basnet R, Rahman S, Sharma M M, Upreti D, Nabi M R U, Kryvyi S, Sakon J, Mortazavi M, Da B, Churchill H and Hu J 2025 *Phys. Rev. B* **111** 014431